Obrabotka metallov (tekhnologiya, oborudovanie, instrumenty) = Metal Working and Material Science. 2023 vol. 25 no. 1 pp. 110–130
ISSN: 1994-6309 (print) / 2541-819X (online)
DOI: 10.17212/1994-6309-2023-25.1-110-130

NSTU NETI

Obrabotka metallov -
Metal Working and Material Science

Journal homepage: http://journals.nstu.ru/obrabotka_metallov

Study of the properties of silicon bronze-based alloys printed using electron beam additive manufacturing technology

Andrey Filippov [a, *], *Ekaterina Khoroshko* [b], *Nikolay Shamarin* [c], *Evgeny Kolubaev* [d], *Sergei Tarasov* [e]

Institute of Strength Physics and Materials Sciences SB RAS, 2/4, pr. Akademicheskii, Tomsk, 634055, Russian Federation

[a] https://orcid.org/0000-0003-0487-8382, avf@ispms.ru, [b] https://orcid.org/0000-0001-9078-5662, eskhoroshko@gmail.com,
[c] https://orcid.org/0000-0002-4649-6465, shnn@ispms.ru, [d] https://orcid.org/0000-0001-7288-3656, eak@ispms.ru,
[e] https://orcid.org/0000-0003-0702-7639, tsy@ispms.ru

ARTICLE INFO

Article history:
Received: 20 January 2023
Revised: 25 January 2023
Accepted: 01 February 2023
Available online: 15 March 2023

Keywords:
Additive technologies
Silicon bronze
Structure
Phase composition
Mechanical properties
Corrosion
Friction

Funding
This research was funded by Russian Science Foundation project № 21-79-00084, https://rscf.ru/project/21-79-00084/.

Acknowledgements
Research were conducted at core facility "Structure, mechanical and physical properties of materials".

ABSTRACT

Introduction. Additive technologies make it possible to curb material expenses by reducing allowances for the final dimensional machining of workpieces. For such expensive materials as copper and copper alloys, this method is considerably attractive from a perspective of increasing resource efficiency in production. The operational properties of the C65500 alloy manufactured using additive technologies have not been fully studied and require additional research. **The aim of the work** is to study the structural and phase state, mechanical and operational properties of C65500 bronze specimens printed using electron beam additive manufacturing technology. **In the work**, specimens made of C65500 wire with different heat input values are studied, some of which were subjected to thermal treatment and mechanical processing, as well as specimens, manufactured using multi-wire technology. **The work uses such research methods** as the study of corrosion resistance of bronze specimens using a potentiostat, confocal laser scanning microscopy, friction tests and X-ray phase analysis. **Results and discussion.** Processing of specimens by plastic deformation (compression) and subsequent annealing leads to the most serious structural changes. Based on X-ray phase analysis, it is found that higher silicon content is observed in the case of the addition of silumins to bronze. The study of mechanical properties shows that the specimens, printed using multi-wire technology, have the highest strength properties. During tribological testing, fluctuations in the value of the friction coefficient are revealed, due to the scheme of the experiment and the combined adhesive-oxidative mechanism of specimens' wear. The addition of 10 wt.% aluminum filament to bronze in the additive manufacturing process is an effective means for increasing the resistance of the material to electrochemical corrosion and increasing its wear resistance.

For citation: Filippov A.V., Khoroshko E.S., Shamarin N.N., Kolubaev E.A., Tarasov S.Yu. Study of the properties of silicon bronze-based alloys printed using electron beam additive manufacturing technology. *Obrabotka metallov (tekhnologiya, oborudovanie, instrumenty) = Metal Working and Material Science*, 2023, vol. 25, no. 1, pp. 110–130. DOI: 10.17212/1994-6309-2023-25.1-110-130. (In Russian).

Introduction

Silicon bronzes are rather expensive materials used commonly for the manufacture of products that should possess enhanced corrosion and wear resistance [1]. In connection with this, the development of methods that allow improving the resource usage efficiency is an important scientific and technical task. In this direction, additive manufacturing can provide various options for solving the problem of reducing

*** Corresponding author**
Filippov Andrey V., Ph.D. (Engineering), Head of Laboratory
Institute of Strength Physics and Materials Sciences SB RAS
2/4, pr. Akademicheskii,
634055, Tomsk, Russian Federation
Tel.: 8 (999) 178-13-40, **e-mail:** avf@ispms.ru

the production costs, due to a significant reduction in allowances for the final dimensional machining of workpieces [2]. At the same time, one of the main problems in the additive manufacturing made of copper and its alloys is the oxidation of interlayer boundaries, which significantly worsens the physical and mechanical properties of printed products. In this regard, three-dimensional printing should be carried out either in a protective gas or in a vacuum [3].

An important advantage of additive technologies is the ability to control the printing modes, which allows varying the melting conditions of the material in a wide temperature range. This is especially important in the manufacture of three-dimensional curved products and non-uniform wall thickness. Indeed, the thickness and height of the wall, as well as the total volume of the printed material, significantly affect the heat removal [4] and, accordingly, the formation of the melt bath.

The wire-feed electron-beam additive manufacturing is carried out in a vacuum using a thin wire as a filament. This type of filament is less expensive than powder, which makes this technology less expensive. In addition, this technology allows the use of several wires to feed it into the printing zone in different ratios. As a result, it becomes possible to print new multicomponent alloys with different alloying elements, as well as alloys and composites from dissimilar materials [5–8].

The electron-beam additive manufacturing (*EBAM*) is used to obtain products from nickel heat-resistant alloys [9–12], intermetallic compounds such as *TiAl* [13–15], soft magnetic materials based on iron [16], aluminum alloys [17, 18], and magnesium alloys [19], as well as bronze [20, 21].

In the native industry, the silicon bronze grade *C65500* is of the most common use. It is used in parts intended to chemical industry, aviation, automotive and shipbuilding industries. At the same time, its analogue is known containing ~7 wt.% *Al* and ~2 wt.% *Si* that is produced abroad. This alloy has higher performance characteristics compared to *C65500*. Therefore, obtaining analogues of this alloy is an urgent task. To solve it a technology of the multiwire electron beam additive manufacturing can be used, which is implemented by feeding two or more wires to the melt bath. In the context of obtaining alloys of the *Cu–Al–Si* system, it is possible to use an aluminum filament and feed it in the process of printing bronze in a ratio of 10:1, which should provide the required composition of the alloy. Previously, the multiwire electron-beam additive manufacturing was successfully used to obtain specimens from the *C65500* alloy [22] and the alloy of the *Cu–Al– Si–Mn* system [23]. However, in the works known to date, the operational properties of this alloy, obtained using additive technologies, have not been fully investigated. The properties of alloys printed on the basis of silicon bronze with the addition of aluminum filament also remain unexplored. Varying the *EBAM* heat input, conducting the post-deposition heat and thermomechanical treatments as well as alloying the bronze with *Al-Si* alloys are in fact three different approaches to the structure modification, which are based on altering cooling rate, recrystallization and constitutional undercooling, respectively.

The aim of the work is to study the structural and phase state, mechanical and operational properties of *C65500* bronze specimens printed using electron beam additive manufacturing technology.

Research methodology

The thin-walled specimens were made using the electron-beam additive manufacturing as shown in Figure 1.

Two groups of specimens were obtained by *EBAM*. The first one was made from wire *C65500* with different heat inputs: *mode 1* – 0.19 kJ/mm, *mode 2* – 0.25 kJ/mm, *mode 3* – 0.31 kJ/mm. Some of these specimens, with the most coarse-grained structure, were subjected to thermal (annealing at 850 °C) and mechanical treatment (compression deformation by 10 % and subsequent annealing at 850 °C), which made it possible to successfully change its structural state. More detailed information about the processing modes and the structural state of these specimens is given elsewhere [22].

The second part of the specimens was made using the multiwire technology. This approach was used to change the composition of specimens and assess the possibility of controlling its structure and properties, as well as to obtain an alloy of the *Cu–Al– Si* system with a composition close to foreign analogues (alloy *C64200*) used in aviation and marine engineering. To do this, two wires were fed into the melt bath so that

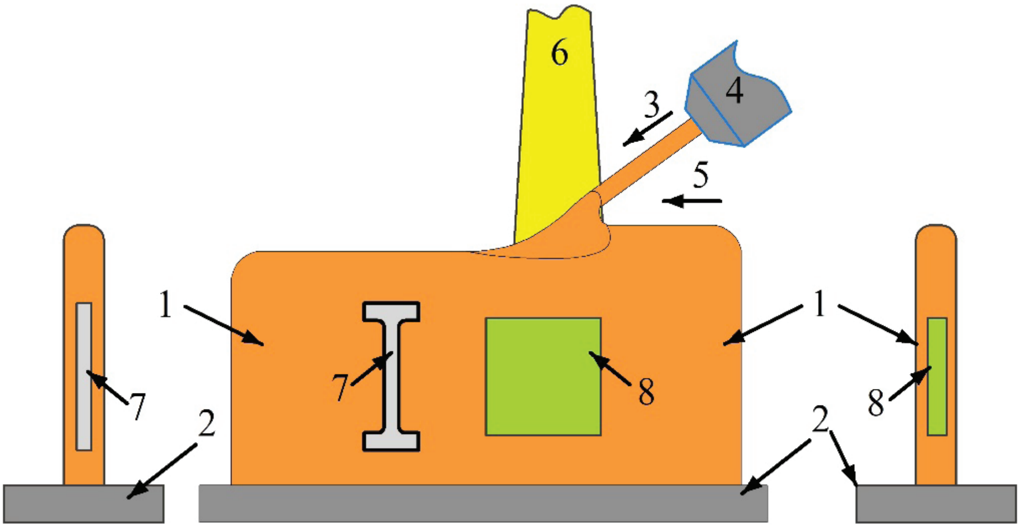

Fig. 1. Scheme of electron beam additive manufacturing and cut-up sketch: *1* – printed material; *2* – substrate; *3* – wire feed direction; *4* – wire feeder; *5* – printing direction; *6* – electron beam; *7* – tensile test specimens; *8* – friction and corrosion resistance test specimen

the first one was constantly the *C65500* itself while the second was made of an alloy to be intermixed with bronze. Commercially pure aluminum (99% *Al*) and *AK5* (*Al-5Si*) and *AK12* (*Al-12Si*) alloys were used as such additives. The both wires' feed rates were adjusted in such a way as to ensure the addition of 10 wt.% of aluminum to the *C65500* alloy. As a result, three alloys were obtained: 1) *C65500* + 10 wt.% *Al*, 2) *C65500* + 10 wt.% *Al-5Si* and 3) *C65500* + 10 wt.% *Al-12Si*. The technique for printing specimens is described in more detail elsewhere [23].

Corrosion resistance of bronze specimens was studied by conducting potentiodynamic tests on a three-electrode circuit and using a potentiostat *Electrochemical Instrument P-45X*. An aqueous solution of 3.5% *NaCl* was used as a corrosive medium. As a result, polarization curves were obtained that reflected the changes in potential and corrosion current. The polarization resistance is calculated basing on the *Butler-Volmer* equation:

$$Rp = (\beta_a\beta_c)/(2.303 I_{\mathrm{corr}}(\beta_a + \beta_c)), \tag{1}$$

where β_a is the slope of the anode branch, β_c is the slope of the cathode branch, i_{corr} is the corrosion current.

The weight loss of the specimens was assessed using a *Sartorius CP 124 S* analytical balance.

The surface of bronze specimens after the corrosion resistance test was examined using a confocal laser scanning microscope *Olympus OLS-4100*. To perform both qualitative and quantitative assessments of the corrosion damage to the surface, optical images were obtained and the roughness was evaluated.

Sliding tests were carried out using a *Tribotechnic* tribometer according to the ball-on-disk scheme under conditions of reciprocating dry sliding friction. Plates cut from printed bronze walls were used as specimens (see Figure 1. pos. 8). Balls made of hardened steel *AISI 52100* were used as counterbodies. The study of the surface of bronze specimens and balls after friction, as well as the measurement of the cross-sectional profile of the wear tracks, was carried out using a confocal laser scanning microscope *Olympus OLS-4100*.

Microhardness was measured using a *Duramin-5* hardness tester at a load of 50 N. The tensile strength characteristics were evaluated on a *Testsystem 110 M-10* testing machine.

The study of the phase composition of bronze specimens was carried out on a *DRON-7* X-ray diffractometer. The elemental composition was determined using *Octane Elect* energy dispersive spectral (*EDS*) analysis on a *Thermo Fisher Scientific Apreo S LoVac* scanning electron microscope.

Metallographic studies of the structure of bronze specimens were performed using a confocal laser scanning microscope *Olympus OLS -4100*.

Results and discussion

Metallographic studies of the structure of specimens

Changing the heat input naturally affected the structure of the as-manufactured *specimens*. As the heat input increases, the grains grow and its shape changes. With minimal heat input (0.19 kJ/mm), a bimodal structure with small elongated and equiaxed grains is observed (Fig. 2, *a*). The medium and high heat input levels 0.25 kJ/mm and 0.31 kJ/mm resulted in forming zigzag-shaped (Fig. 2, *b*) and large columnar grains (Fig. 2, *c*), respectively. Annealing of the columnar grained specimens resulted in forming large non-equiaxed grains with numerous annealing twins (Fig. 2. *d*). Annealing of the pre-deformed by compression specimens led to the most serious structural changes with formation of small equiaxed grains with a large number of annealing twins (Fig. 2, *e*).

The change in the structural state of the specimens is due to differences in the temperature gradient during printing. With low heat input, the crystallization rate increases and as a result, a finer-grained microstructure is formed. In turn, annealing, as well as deformation and subsequent annealing, lead to recrystallization of the material [24, 25].

As a result of printing of the *C65500* alloy with the addition of 10 wt.% *Al*, a fine-grained structure with almost equiaxed grains 25–125 μm in size was formed (Fig. 3, *a*). Annealing twins and secondary phase inclusions are also observed. When printing with the addition of alloys *Al-5Si* and *Al-12Si*, the structure of the specimens looks different. In both cases, dendritic structure is formed (Figs. 3, *b* and *c*). Dendrites' first order axes are oriented along the direction of wall building, and in the interdendritic space there are interlayers of the secondary phase with a thickness of 3–15 μm.

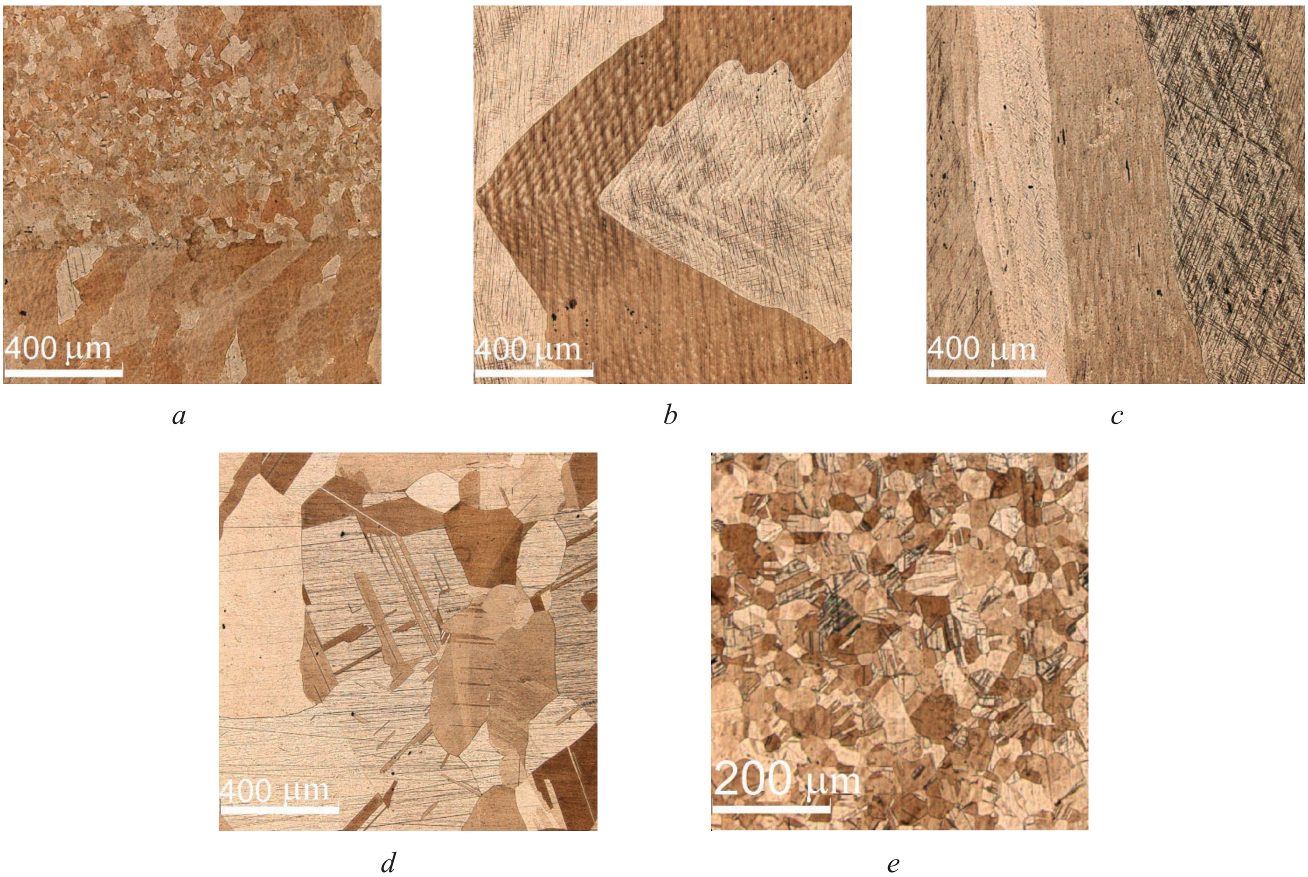

Fig. 2. Typical microstructure of specimens printed from *C65500*. Printing modes 1 (*a*), 2 (*b*) and 3 (*c*). Specimens after annealing (*d*), as well as after deformation and subsequent annealing (*e*)

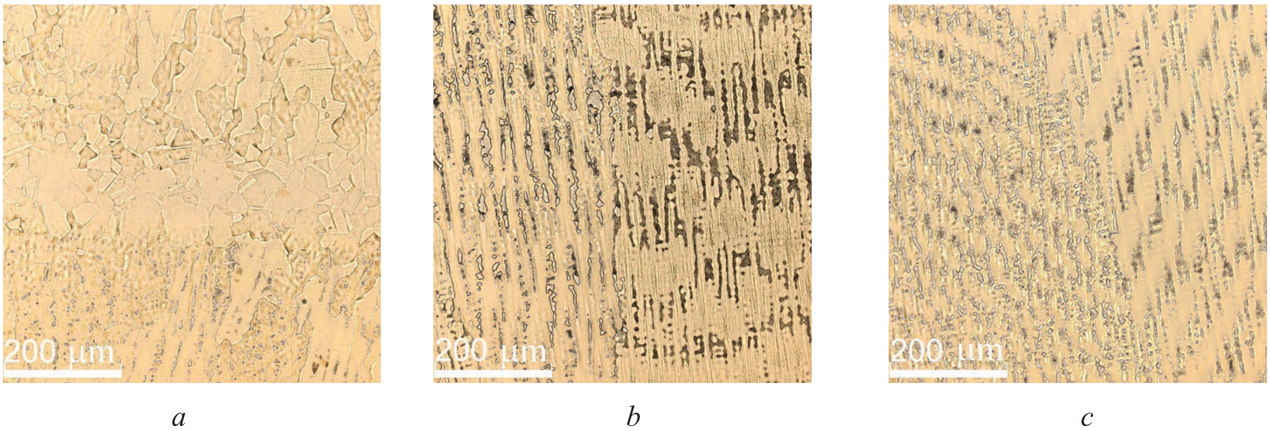

Fig. 3. Typical microstructure of specimens printed from *C65500* with the addition of 10 wt.% *Al* (*a*), 10 wt.% *Al–5Si* (*b*) and 10 wt.% *Al-12Si* (*c*)

XRD and EDS analysis phase composition samples

It was established from the results of X-ray phase analysis that all the studied specimens were mainly composed of the α-*Cu* solid solution (Fig. 4). The specimens printed with the addition of aluminum filaments additionally contained iron and particles of silicon silicide that were formed due to the presence of iron in the *Al-Si* wires.

According to the known phase diagrams [26–31], alloys of the *Cu–Al–Si* system can have two phases, namely, *FCC* α-*Cu* phase and *HCP* γ-phase. In the samples under consideration, it was found using the *EDS* that the secondary γ-phase contains (copper-balance) ~7 at.% *Al*, ~(9–10)at. % *Si* and ~(0.5–0.6) at.% *Mn*, while the α-phase contains ~10 at.% *Al*, ~(3.5–5) at.% *Si* and ~(1.2–1.5) at.% *Mn*. The higher silicon content is observed obviously in the case of the adding of silumins to the bronze.

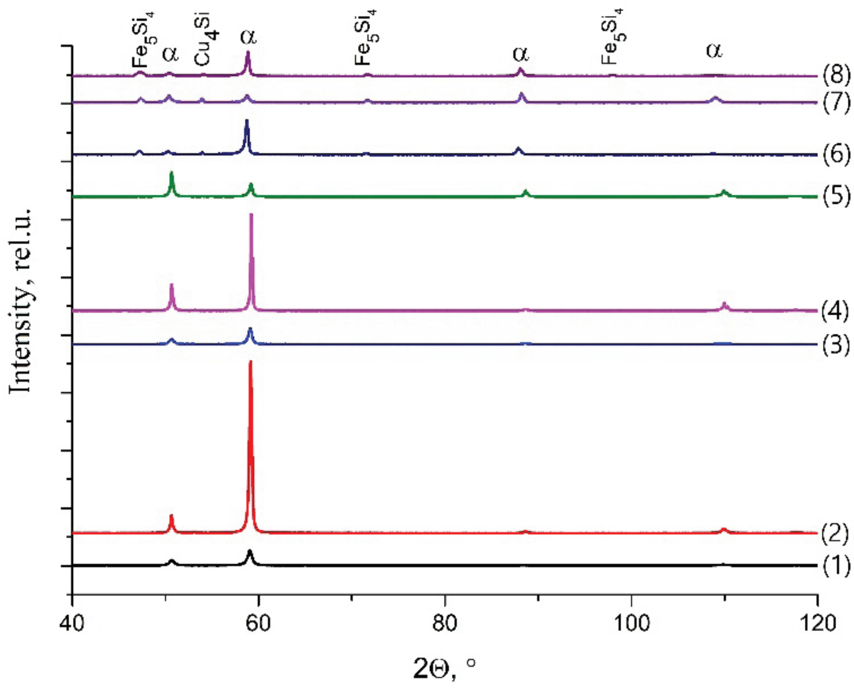

Fig. 4. X-ray diffraction patterns of specimens printed from *C65500* and with the addition of aluminum filament. Printing modes 1 (1), 2 (2) and 3 (3). Specimens after annealing (4), deformation and subsequent annealing (5). Specimens with the addition of 10 wt.% *Al* (6), 10 wt.% *Al–5Si* (7) and 10 wt.% *Al-12Si* (8)

Mechanical properties of specimens

Changing the heat input, the use of thermal and mechanical treatments, as well as alloying with aluminum through the use of multiwire technology, made it possible to obtain bronze specimens not only with different structures, but also with modified mechanical properties. It can be seen that the specimens printed using the multiwire technique have the highest strength (Table 1). In addition, these specimens (with the exception of the *C65500* alloy with the addition of 10 wt.% *Al*) are characterized by sufficiently high ductility. Consequently, the two-phase structure of the specimens printed with the addition of *Al-5Si* and *Al-12Si* alloys is characterized by high strength and simultaneously high ductility. More detailed study of the strength of the specimens under consideration is presented [22, 23].

Table 1

Mechanical properties of specimens printed from *C65500* and with the addition of aluminum filament

Specimen designation	Offset yield strength, MPa	Ultimate strength, MPa	Strain-to-fracture, %
C65500 (mode 1)	89	242	83
C65500 (mode 2)	93	294	75
C65500 (mode 3)	82	253	114
C65500 (annealing)	92	301	76
C65500 (deformation + annealing)	75	318	91
C65500 (10 wt.% *Al*)	203	434	21
C65500 (10 wt.% *Al–5Si*)	150	394	67
C65500 (10 wt.% *Al–12Si*)	186	448	57

Structural modifications have also affected the microhardness of the specimens (Fig. 5). Heat treatment expectedly reduced the microhardness due to the removal of residual stresses. As in the case of strength, specimens with a two-phase structure have a higher hardness compared to that of the single-phase ones. The increase in microhardness was 140–215 %.

Corrosion

The above-described differences in the structural and phase states of the studied specimens affected not only its mechanical properties, but also its corrosion resistance. Figure 6 shows the potentiodynamic polarization curves that were recorded during the study of the electrochemical corrosion. In all the cases under consideration, the potential changes in the cathode part of the curves are without any significant fluctuations. In the anodic part of the curves, the potential changes similarly to that of the cathodic one, but there is a small region with a slowing growth in the potential, which may indicate passivation of the specimen's surface. For a specimen, subjected to pre-deformation and annealing, this section is the longest (Fig. 6a). Therefore, this specimen is the most resistant to the action of the corrosive media, which can be caused by more active formation of aluminum and copper oxides, which hinder the anodic dissolution of the specimen. Such an increase in chemical activity may be the result of a refinement of the material structure, accompanied by an increase in the length of grain boundaries. The boundaries serve as a source of active ions that react with the solution in the electrochemical cell and form passive oxide films. In addition, the results obtained indicate the absence of pitting on the surface of all specimens.

The parameters of the electrochemical potential of the specimens were established. The corrosion potential (Table 2) for specimens printed with low (mode 1), medium (mode 2) and high (mode 3) heat input are as follows: –178 mV, –210 mV and –202 mV, respectively. The post-manufacture annealing of both as-

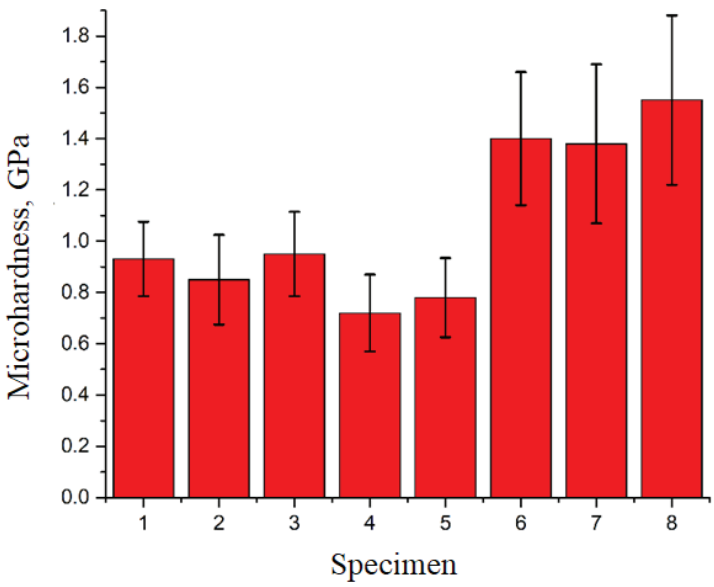

Fig. 5. Microhardness of specimens printed from *C65500* and with the addition of aluminum filament. Printing modes 1 (1), 2 (2) and 3 (3). Specimens after annealing (4), deformation and subsequent annealing (5). Specimens with the addition of 10 wt.% *Al* (6), 10 wt.% *Al–5Si* (7) and 10 wt.% *Al–12Si* (8)

manufactured and pre-deformed specimens leads to a decrease in the value of the corrosion potential. The corrosion current for this group of specimens does not change significantly (from 5.5 to 5.74 μA).

The potentiodynamic polarization curves for the second group of specimens printed with the addition of an aluminum filament are shown in Figure 6, *b*. By its nature, it is similar to those of the as-printed silicon bronze specimens (Fig. 6, *a*). An exception is a specimen printed with the addition of *Al-12Si* alloy. In this case, no surface passivation area is observed, and anodic dissolution begins immediately. For these specimens the corrosion potential ranges from –193 mV to –251 mV, which is generally close in magnitude to that of as-printed silicon, bronze (Table 2). The value of the corrosion current for the specimen *C65500* + 10 wt.% *Al-5Si* is the smallest, and for samples *C65500* + 10 wt.% *Al* and *C65500* + 0 wt.% *Al-12Si* is the largest among those considered in this work.

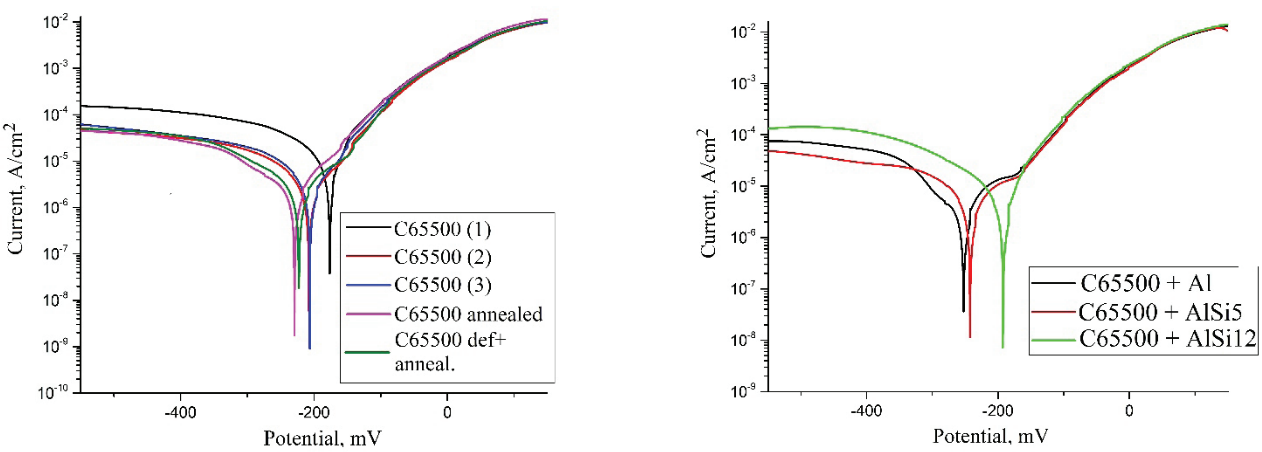

a *b*

Fig. 6. Polarization curves for specimens printed from *C65500* (*a*) and with the addition of aluminum filament (*b*)

Table 2

Parameters of *Taffel* curves according to the data of potentiodynamic tests of specimens printed from *C65500* and with the addition of aluminum filament

Specimen designation	Parameters of polarization curves				
	E_{corr}, mV	I_{corr}, μA	βa	βc	*Rp*, kOhm
C65500 (1)	–178	5.54	0.030371	–0.02667	1.7
C65500 (3)	–210	5.74	0.067731	–0.05687	2.7
C65500 (7)	–202	5.6	0.064345	–0.08164	2.4
C65500 (annealing)	–229	5.71	0.069095	–0.10014	1.7
C65500 (deformation + annealing)	–223	5.5	0.110449	–0.13455	4.8
C65500 (10 wt.% *Al*)	–251	6.6	0.168932	–0.12941	3.6
C65500 (10 wt.% *Al–5Si*)	–239	5.2	0.246156	–0.18557	6.3
C65500 (10 wt.% *Al–12Si*)	–193	8.4	0.116204	–0.13008	5.6

A quantitative assessment of the corrosion resistance can be obtained by calculating the polarization resistance using equation (1) from the polarization curves. The value of *Rp* characterizes how resistant the specimen is to oxidation with respect to the applied potential. Based on the data obtained, it follows that the annealing the pre-deformed specimens contributes to an increase in the polarization resistance of specimens printed from silicon bronze. In turn, when printing specimens with the addition of aluminum filaments, the most effective in terms of increasing the polarization resistance is the addition of *Al-5Si* alloy.

For a more detailed assessment of the effect of a corrosive medium on the surface of the specimens, it has been analyzed using a laser scanning microscope. After testing, a micro-topology pattern formed on the surface of the specimens, with clearly distinguishable individual structural elements (grains, annealing twins, etc.). Pitting marks on the surfaces of silicon bronze (Fig. 7) and bronzes printed with the addition of aluminum filament (Fig. 8) were not detected. The boundaries of grains and annealing twins did not undergo any significant dissolution.

At the same time, the visually observed surface pattern is not the same in all cases. To quantify these differences, the surface roughness of the specimens under study was evaluated. From the data obtained, it can be seen that the specimens printed from bronze *C65500* after testing (Fig. 9) are characterized by the most significant surface roughness. The use of high-temperature annealing contributed to the decrease in the arithmetic mean value of the asperity height (*Ra*) by 6–12 %. The smallest roughness is observed on the corroded surface of the pre-deformed and annealed specimen (*Ra* = 0.275 μm).

The multiwire approach had its effect on the corroded surface roughness. Based upon the data obtained, the least surface roughness (*Ra* = 0.296 μm) is exhibited by the specimen printed with the addition of *Al-5Si* alloy. Based on the data obtained, it follows that the surfaces of the specimens with the lowest roughness are oxidized more uniformly, which may indicate its higher resistance to the electrolyte.

Another quantitative characteristic of corrosion resistance of specimens is the loss of mass. To obtain it, the specimens were weighed on an analytical balance before and after testing. As a result, the mass loss was determined for all the studied specimens (Fig. 10). High-temperature annealing, as well as annealing the pre-deformed specimens caused the reduction in mass loss by 15–30% in comparison the that of as-printed silicon bronze specimens. The addition of aluminum filament made it possible to further reduce the weight loss of as-printed specimens by 13–31 % with regard to both as-printed and annealed specimens of bronze *C65500*.

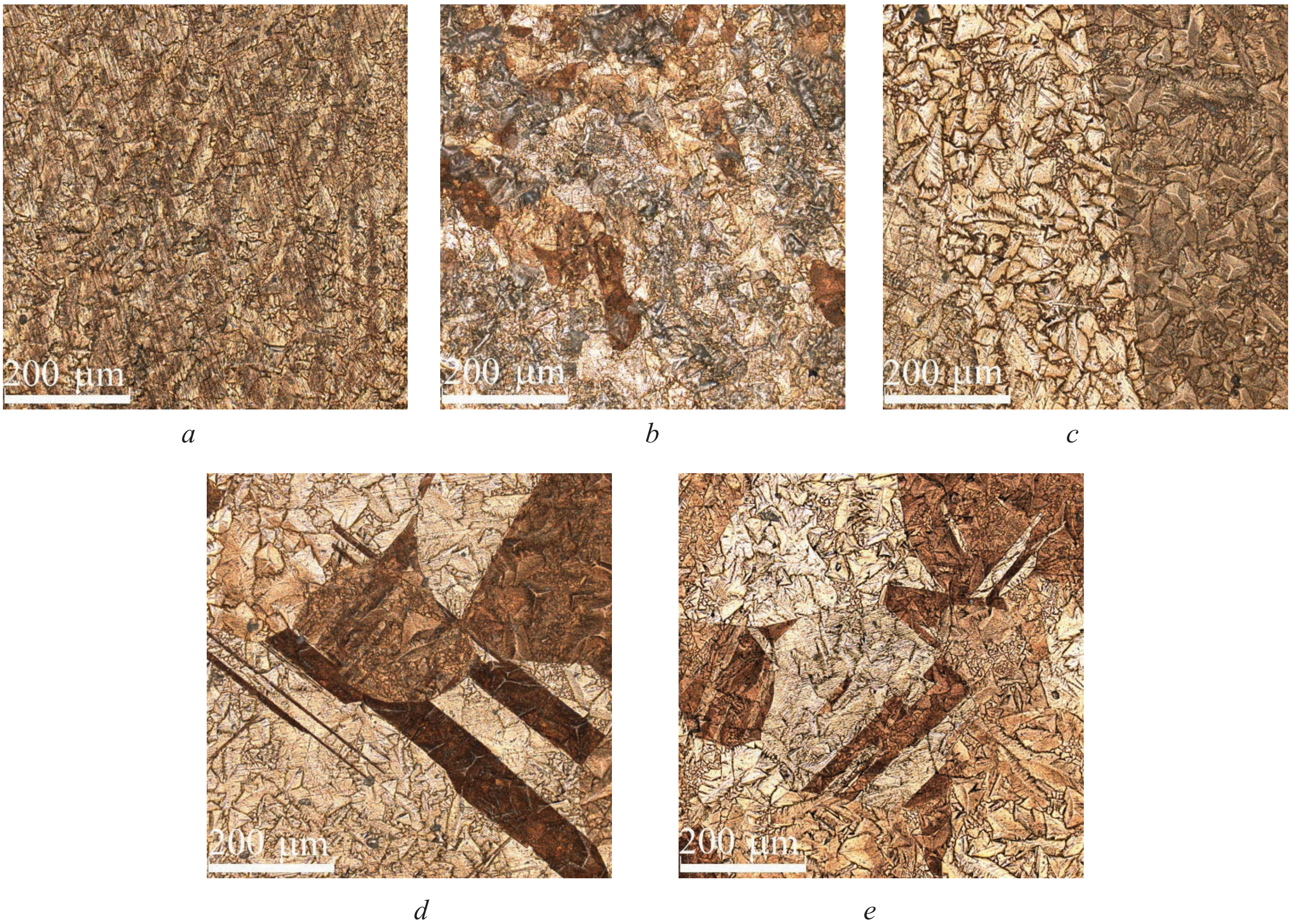

Fig. 7. The surface of *C65500* specimen, printed by the *EBAM* method, after corrosion tests. Printing modes 1 (*a*), 2 (*b*) and 3 (*c*). Specimen after annealing (*d*), deformation and subsequent annealing (*e*)

Fig. 8. The surface of *C65500* specimen with the addition of 10 wt.% *Al* (*a*), 10 wt.% *Al–5Si* (*b*) and 10 wt.% *Al–12Si* (*c*) after corrosion tests

All of these results consistently indicate the improved corrosion resistance of the bronze specimens with structures modified due to the use of mechanical and thermal treatments. In turn, the addition of the *Al-5Si* alloy is the most effective means for modifying the material in order to increase its resistance to electrochemical corrosion.

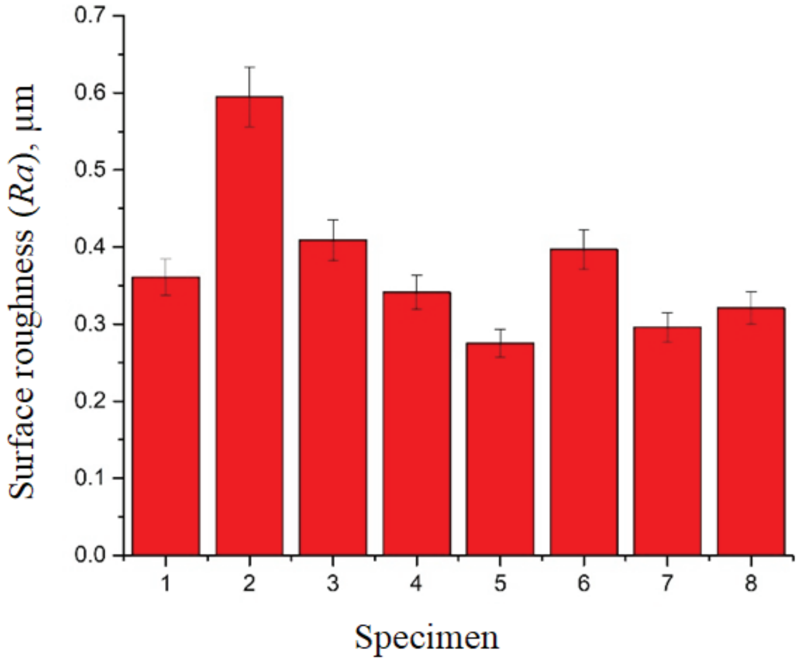

Fig. 9. Surface roughness after electrochemical corrosion of the *C65500* specimen with the addition of aluminum filament. Printing modes 1 (1), 2 (2) and 3 (3). Samples after annealing (4), deformation and subsequent annealing (5). Samples with the addition of 10 wt.% *Al* (6), 10 wt.% *Al–5Si* (7) and 10 wt.% *Al–12Si* (8)

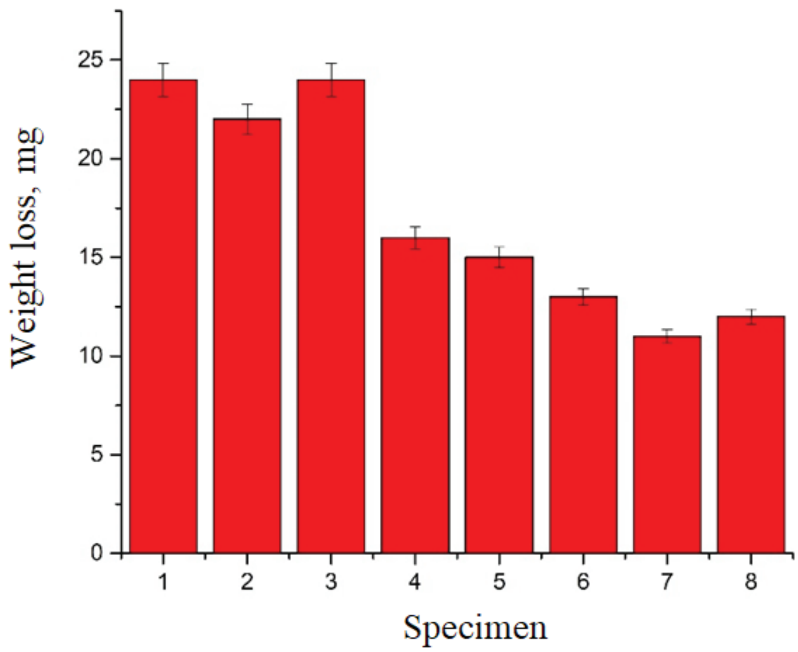

Fig. 10. Mass loss after electrochemical corrosion of the *C65500* specimen with the addition of aluminum filament. Printing modes 1 (1), 2 (2) and 3 (3). Samples after annealing (4), deformation and subsequent annealing (5). Samples with the addition of 10 wt.% *Al* (6), 10 wt.% *Al–5Si* (7) and 10 wt.% *Al–12Si* (8)

Tribological tests

The change in the structural and phase state, as well as in the mechanical properties, also affected the results of testing the specimens for friction and wear. From the beginning of testing, the coefficient of friction coefficient (*CoF*) values are high for bronze *C65500* specimens printed with different heat inputs (Fig. 11). Then it decreases by about 20%, after which it begins to increase monotonically until reaching the previous high values. During sliding of a specimen with a structure formed as a result of high-temperature annealing, significant fluctuations in the value of *CoF* are observed (reach an amplitude of ~0.2) and occupy most of the test time. Sliding of the pre-deformed and annealed specimen shows the *CoF* oscillations at the final stage of testing as high as ~0.25. The average *CoF* values of specimens printed with low (mode 1), medium (mode 2) and high (mode 3) heat input are 0.52, 0.39 and 0.29, respectively. For the specimen after high-temperature annealing, the *CoF* is 0.3, and for the sequentially deformed and annealed it is 0.34. The high amplitude of the *CoF* fluctuations is partly due to the test scheme. With reciprocating sliding, the sliding speed is not a constant value in all sections of the friction track. Upon reaching the final section of the friction track, it tends to zero, and then quickly recovers at the start of motion in each new sliding cycle. As a result, a slight change in friction conditions occurs at the extreme sections of the friction track, which affects the magnitude of the friction force.

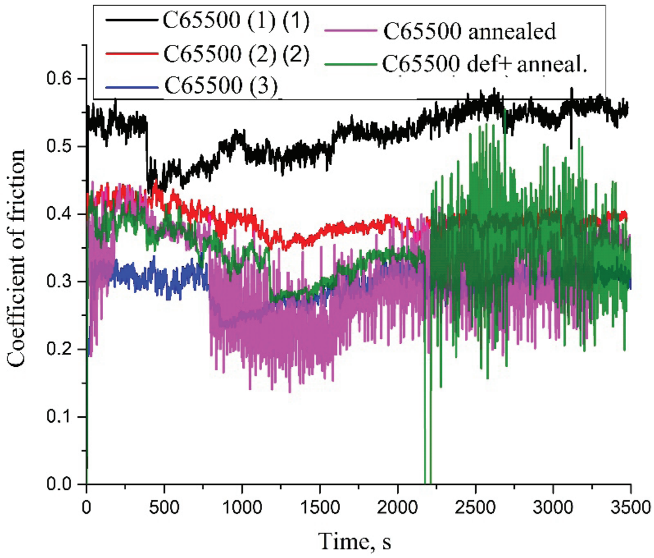

Fig. 11. Change in the value of the coefficient of friction during tribological tests of *C65500* specimens

During sliding of specimens printed with the addition of aluminum filament, a different character of the change in the coefficient of friction is observed (Fig. 12). In the beginning, the *CoF* increases for ~150 seconds, which may correspond to a running-in period, and then stabilizes at a certain level. At the same time, the *CoF* value significantly decreased in comparison with that of bronzes printed without aluminum additives. The average *CoF* value is 0.184, 0.28 and 0.191 in the friction of bronze specimens printed with the addition of 10 wt.% *Al*, *Al-5Si* and *Al-12Si*, respectively.

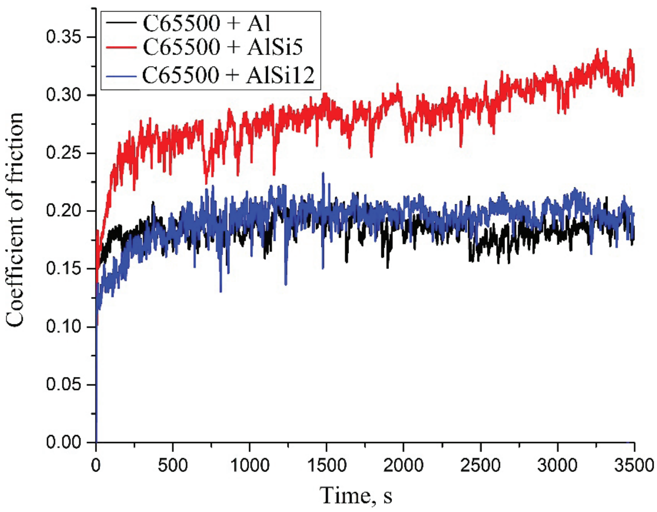

Fig. 12. Change in the value of the coefficient of friction during tribological tests of *C65500* specimens, printed with the addition of aluminum filament

To explain the reasons for the *CoF* fluctuations, the surfaces of wear tracks on bronze specimens (Figs. 13, 15) and the surfaces of steel balls (Figs. 14, 16) were examined. On the surface of the as-printed bronze *C65500* specimens, the pronounced wear tracks were formed and the surfaces of these tracks were covered with dark oxides and traces of mechanical damage. On the periphery, traces of deformation of individual sections of the material are also visible; this indicates plastic deformation of the specimens under the action of the counterbody during sliding friction.

No signs of wear were found on the surfaces of the steel balls (Fig. 13), which is natural due to its significantly higher hardness compared to those of specimens printed from *C65500* bronze. At the same time,

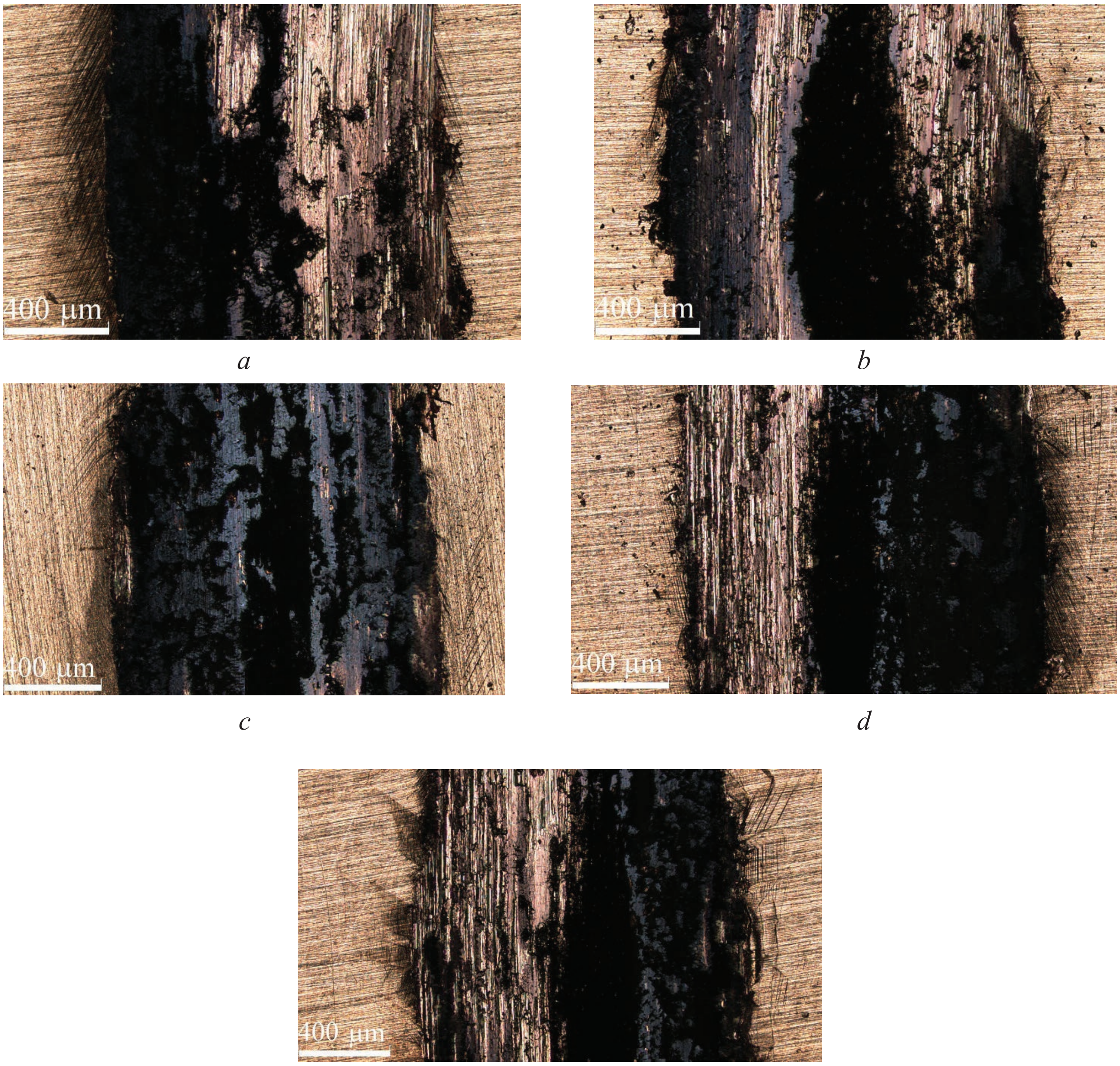

Fig. 13. Images of the wear surfaces of *C65500* bronze specimens, printed according to 1 (*a*), 3 (*b*) and 7 (*c*) *EBAM* modes, annealed specimen (*d*), deformed and annealed specimen (*e*)

the marks of bronze adhered to balls' surface are observed. This is due to the adhesive wear mechanism in the considered steel-bronze friction pair. The thickness of these adhesion transferred layers does not exceed 1.5 µm, which was established from measurement of a three-dimensional surface profile using laser scanning microscopy.

The surface of wear tracks of bronze specimens (Fig. 15), printed with the addition of aluminum filament, significantly differs from those of the tracks on the surface of as-printed bronze specimens *C65500* (Fig. 13). There are no traces of plastic deformation of the material at the periphery of the tracks; there is also no surface oxidation in the form of dark spots. At the same time, on the periphery of the tracks there are areas with material pushed aside as a result of deformation. The surface of the balls (Fig. 16) is covered with a layer of adhesion-transferred bronze, which is significant both in area and in thickness. The thickness of the adhered material is uneven over the entire area and reaches 5–12 µm. This indicates a stronger adhesive interaction between the materials of the friction pair.

The experimental data obtained indicate that in the case of dry reciprocating sliding of the specimens, the *CoF* fluctuations were revealed, which are unavoidable with the use this experimental scheme and the combined adhesive-oxidative wear mechanism.

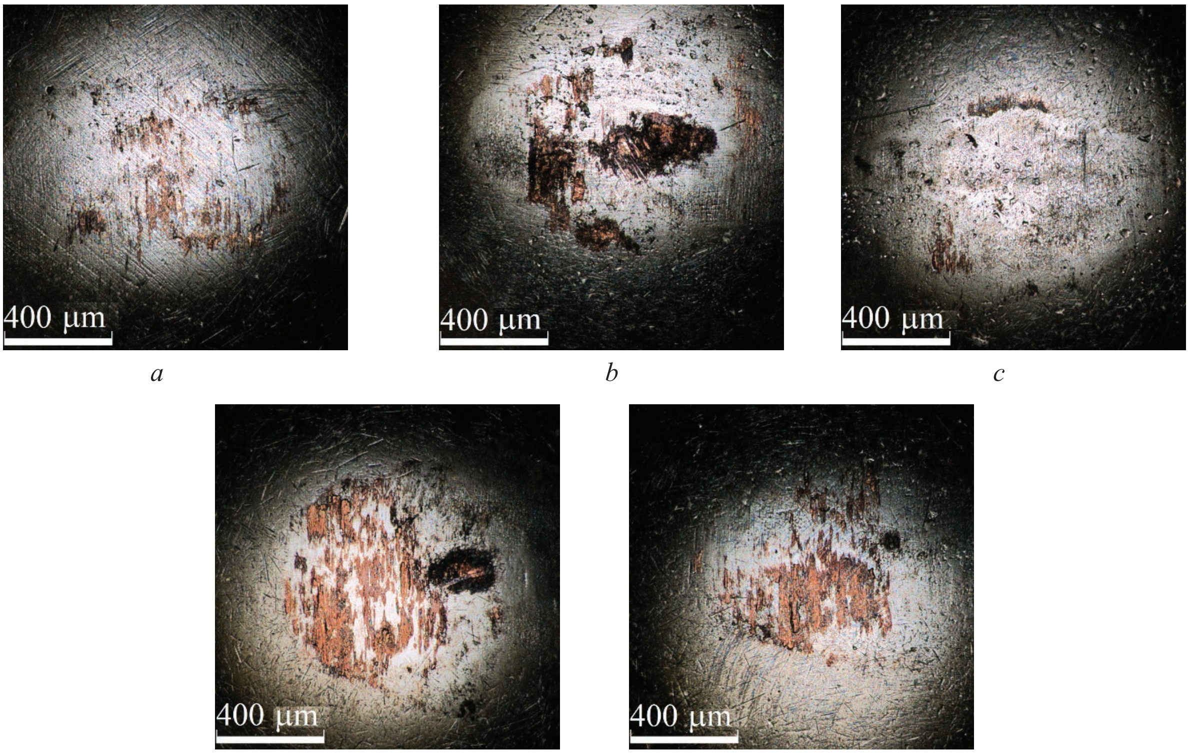

a *b* *c*

d *e*

Fig. 14. Images of the surface of steel balls after friction in a pair with *C65500* bronze specimens, printed according to 1 (*a*), 3 (*b*) and 7 (*c*) *EBAM* modes, annealed specimen (*d*), deformed and annealed specimen (*e*)

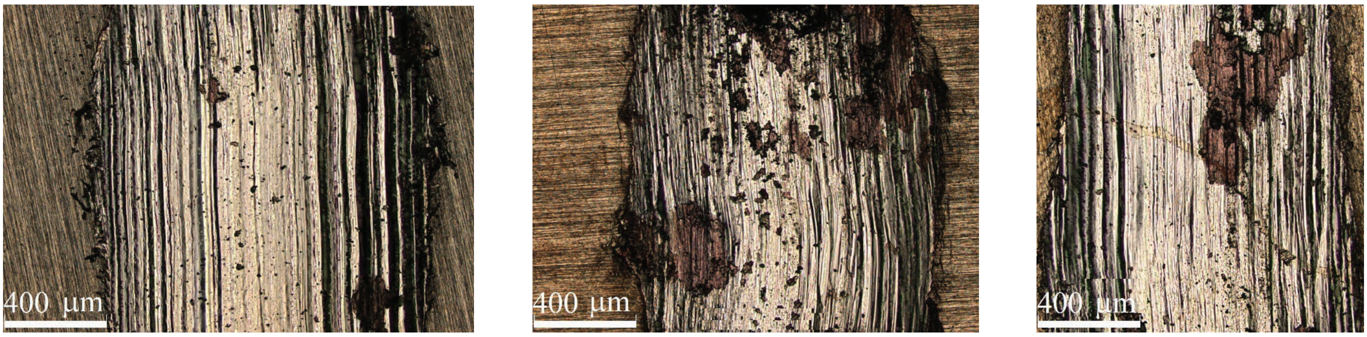

a *b* *c*

Fig. 15. Images of the wear surfaces of *C65500* bronze specimens, printed with the addition of 10 wt.% *Al* (*a*), 10 wt.% *Al–5Si* (*b*) and 10 wt.% *Al–12Si* (*c*)

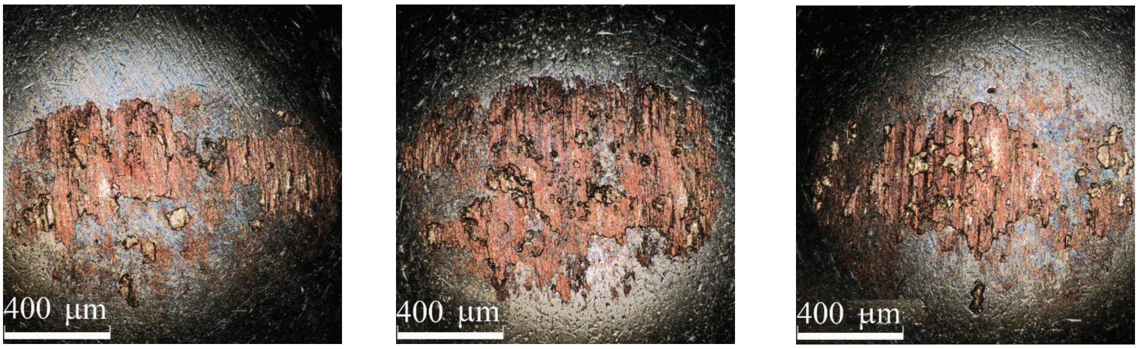

a *b* *c*

Fig. 16. Images of the surface of steel balls after friction in a pair with *C65500* bronze specimens, printed with the addition of 10 wt.% *Al* (*a*), 10 wt.% *Al–5Si* (*b*) and 10 wt.% *Al–12Si* (*c*)

Quantitative determination of the amount of wear was carried out by determining the cross-sectional profile of wear tracks according to the standard *ASTM G133-05* method. To do this, cross-sectional profiles of wear tracks formed on the surfaces of specimens were reconsrtucted for the as-printed bronze *C65500* (Fig. 17, *a*) and bronze with the addition of aluminum filament (Fig. 17, *b*) using the software. The obtained profiles confirm the presence of the material deformation and its displacement to the periphery of the wear tracks. The key feature of the formation of burrs is the relationship between its height and the mechanical properties of the specimens. The most ductile and least hard specimens are more severely deformed during friction and the highest burrs are formed on its surface. Harder specimens printed with the addition of aluminum filament are less prone to plastic deformation during sliding friction, and the height of the burrs formed on its surface is 2–3 times less (10–15 μm) than for specimens made of bronze (20–30 μm).

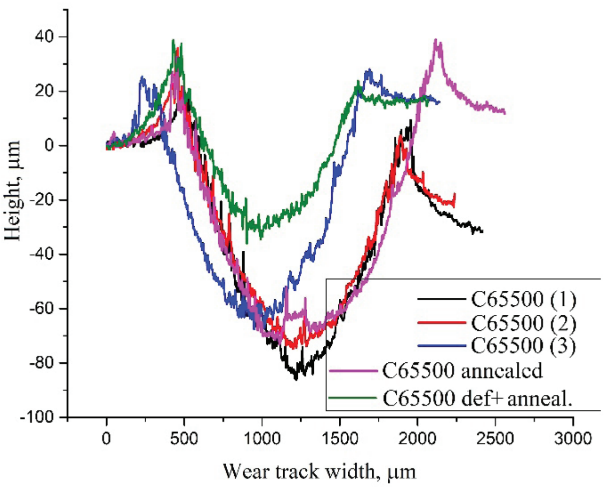

a

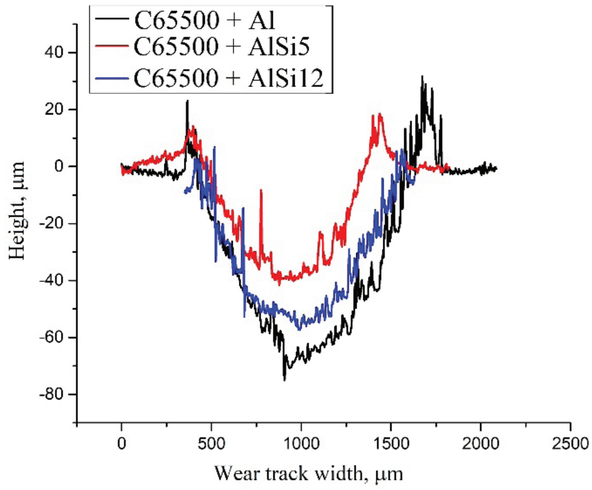

b

Fig. 17. Cross-section profiles of the wear tracks of specimens, printed from bronze *C65500* (*a*) and with the addition of aluminum filament (*b*)

In accordance with the standard method, the cross-sectional areas of the wear tracks were determined. It can be observed from Figure 18, that the largest cross-sectional area of the wear track was formed during testing of the annealed specimens of bronze *C65500* in accordance with its lowest microhardness. As a result, under conditions of microcontact interaction in a friction pair, its material is easier to deform and wear out. In turn, the use of pre-deformation followed by annealing makes it possible to reduce wear by 15–30% for specimens printed from bronze *C65500*. This is ensured by a fine structure, which more effectively resists plastic deformation due to the presence of a large number of grain and twin boundaries. Among the specimens printed with the addition of aluminum filament, the highest wear resistance was obtained when intermixing the bronze with the *Al-5Si* alloy. Its wear is 25% less than that of the most wear-resistant specimen of as-printed bronze *C65500*. This is due to its high microhardness and mechanical strength. The decrease in wear resistance of alloys printed with the addition of aluminum and *Al-12Si* is due to its mechanical properties and phase composition. In the first case, the alloy has low ductility and subsurface fracture is more feasible during sliding. In the second case, the addition of *Al-12Si* to *C65500* greatly increases the amount of silicides, which adversely affect the properties of the alloy. During sliding, these fine silicides can be pulled out of the matrix and then act on the surface as abrasive particles, increasing the wear of the bronze surface. In addition, alloys printed with the addition of aluminum filament are less prone to the formation of oxide layers. Because of this, the protective function of the oxide layers is not fulfilled and wear occurs mainly due to the adhesive mechanism. As a result, despite high mechanical properties and microhardness, wear reduction is not so significant.

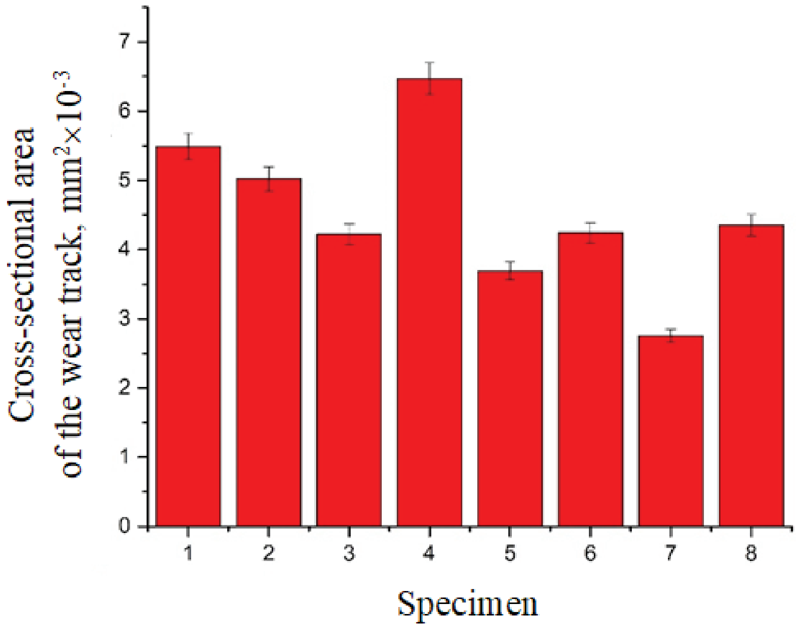

Fig. 18. Cross-sectional area of the wear tracks for specimens printed from bronze *C65500* and with the addition of aluminum filament. Printing modes 1 (1), 2 (2) and 3 (3). Samples after annealing (4), deformation and subsequent annealing (5). Samples with the addition of 10 wt.% *Al* (6), 10 wt.% *Al–5Si* (7) and 10 wt.% *Al–12Si* (8)

Conclusions

The paper presents the results of experimental studies of silicon bronze *C65500*, printed using the technology of electron beam additive manufacturing. Based on the results obtained, the effect of printing conditions and the addition of aluminum filament on the structure, mechanical properties, as well as its relationship with the corrosion resistance and wear resistance of the specimens were established.

1. According to the studies performed, the addition of 10 wt.% aluminum filament leads to the formation of a two-phase structure in printed specimens. In this case, the main phase is the α-*Cu* solid solution with secondary *HCP* γ-phase precipitates. The formation of the two-phase structure contributes to improving the strength by ~1.2–1.9 times and microhardness by ~1.4–2.2 times, as well as impairing the ductility by 1.1–5.4 times compared with single-phase specimens.

3. As a result of the study of corrosion resistance, it is shown that corrosion proceeds without the formation of pitting on the surfaces of silicon bronze and bronzes printed with the addition of aluminum filament.

4. High-temperature annealing, as well as plastic deformation by compression followed by annealing, contributed to a reduction in mass loss by 15–30% for specimens printed from silicon bronze.

5. The addition of aluminum filament made it possible to further reduce the weight loss of printed specimens by 13–31%, relative to specimens printed from bronze *C65500*.

6. The use of deformation followed by annealing makes it possible to reduce wear by 15–30% for specimens printed from bronze *C65500*. This is ensured by a fine structure, which more effectively resists plastic deformation due to the presence of a large number of grain boundaries.

7. The addition of 10 wt.% alloy *Al-5Si* in the process of printing bronze contributed to an increase in the wear resistance of the material by 25%, compared with specimens from bronze *C65500*.

The results obtained can be used in the development of technologies for the additive production of products from silicon bronzes.

References

1. Schütze M., Feser R., Bender R. *Corrosion resistance of copper and copper alloys*. Wiley, 2011. 752 p.

2. Horn T.J., Gamzina D. Additive manufacturing of copper and copper alloys. *Additive Manufacturing Processes*. ASM International, 2020, pp. 388–418. DOI: 10.31399/asm.hb.v24.a0006579.

3. Adler L., Fu Z., Koerner C. Electron beam based additive manufacturing of Fe3Al based iron aluminides – processing window, microstructure and properties. *Materials Science and Engineering A*, 2020, vol. 785, p. 139369. DOI: 10.1016/j.msea.2020.139369.

4. Ledford C., Rock C., Tung M., Wang H., Schroth J., Horn T. Evaluation of electron beam powder bed fusion additive manufacturing of high purity copper for overhang structures using in-situ real time backscatter electron monitoring. *Procedia Manufacturing*, 2020, vol. 48, pp. 828–838. DOI: 10.1016/j.promfg.2020.05.120.

5. Chumaevskii A.V., Kolubaev E.A., Osipovich K.S., GurIanov D.A., Rubtsov V.E., Nikonov S.Y., Boltrushevich A.E. Obtaining of bimetallic product from nickel superalloy and heat-resistant bronze by wire-feed electron beam additive manufacturing. *Russian Physics Journal*, 2022, vol. 65, pp. 1231–1238. DOI: 10.1007/s11182-022-02756-5.

6. Fu Z., Ye J., Franke M., Körner C. A novel approach for powder bed-based additive manufacturing of compositionally graded composites. *Additive Manufacturing*, 2022, vol. 56, p. 102916. DOI: 10.1016/j.addma.2022.102916.

7. Filippov A.V., Khoroshko E.S., Shamarin N.N., Savchenko N.L., Moskvichev E.N., Utyaganova V.R., Kolubaev E.A., Smolin A.Y., Tarasov S.Y. Characterization of gradient CuAl–B4C composites additively manufactured using a combination of wire-feed and powder-bed electron beam deposition methods. *Journal of Alloys and Compounds*, 2021, vol. 859, p. 157824. DOI: 10.1016/j.jallcom.2020.157824.

8. Zykova A., Chumaevskii A., Panfilov A., Vorontsov A., Nikolaeva A., Osipovich K., Gusarova A., Chebodaeva V., Nikonov S., Gurianov D., Filippov A., Dobrovolsky A., Kolubaev E., Tarasov S. Aluminum Bronze/Udimet 500 composites prepared by electron-beam additive double-wire-feed manufacturing. *Materials (Basel)*, 2022, vol. 15, p. 6270. DOI: 10.3390/ma15186270.

9. Gotterbarm M.R., Seifi M., Melzer D., Džugan J., Salem A.A., Liu Z.H., Körner C. Small scale testing of IN718 single crystals manufactured by EB-PBF. *Additive Manufacturing*, 2020, vol. 36, p. 101449. DOI: 10.1016/j.addma.2020.101449.

10. Bäreis J., Semjatov N., Renner J., Ye J., Zongwen F., Körner C. Electron-optical in-situ crack monitoring during electron beam powder bed fusion of the Ni-base superalloy CMSX-4. *Progress in Additive Manufacturing*, 2022. DOI: 10.1007/s40964-022-00357-9.

11. Fortuna S., Gurianov D., Nikonov S., Ivanov K., Mironov Y., Vorontsov A. Features of the macro-, micro-, and fine structure of the nickel superalloy product material formed by the method of electron beam additive manufacturing. *Materials*, 2022, vol. 15, p. 8882. DOI: 10.3390/ma15248882.

12. Gurianov D., Fortuna S., Nikonov S., Kalashnikova T., Chumaevskii A., Utyaganova V., Kolubaev E., Rubtsov V. Assessment of structure and properties homogeneity after repairing of a nickel-based superalloy product by the electron beam additive technology. *Crystals*, 2022, vol. 12, p. 1400. DOI: 10.3390/cryst12101400.

13. Bieske J., Franke M., Schloffer M., Körner C. Microstructure and properties of TiAl processed via an electron beam powder bed fusion capsule technology. *Intermetallics*, 2020, vol. 126, p. 106929. DOI: 10.1016/j.intermet.2020.106929.

14. Knörlein J., Franke M.M., Schloffer M., Körner C. In-situ aluminum control for titanium aluminide via electron beam powder bed fusion to realize a dual microstructure. *Additive Manufacturing*, 2022, vol. 59, p. 103132. DOI: 10.1016/j.addma.2022.103132.

15. Reith M., Breuning C., Franke M., Körner C. Impact of the power-dependent beam diameter during electron beam additive manufacturing: a case study with γ-TiAl. *Applied Sciences*, 2022, vol. 12, p. 11300. DOI: 10.3390/app122111300.

16. Yang J., Fu Z., Ye J., Kübrich D., Körner C. Electron beam-based additive manufacturing of Fe93.5Si6.5 (Wt.%) soft magnetic material with controllable magnetic performance. *Scripta Materialia*, 2022, vol. 210, p. 114460. DOI: 10.1016/j.scriptamat.2021.114460.

17. Utyaganova V., Filippov A., Tarasov S., Shamarin N., Gurianov D., Vorontsov A., Chumaevskii A., Fortuna S., Savchenko N., Rubtsov V., Kolubaev E. Characterization of AA7075/AA5356 gradient transition zone

in an electron beam wire-feed additive manufactured sample. *Materials Characterization*, 2021, vol. 172, p. 110867. DOI: 10.1016/j.matchar.2020.110867.

18. Utyaganova V.R., Filippov A.V., Shamarin N.N., Vorontsov A.V., Savchenko N.L., Fortuna S.V., Gurianov D.A., Chumaevskii A.V., Rubtsov V.E., Tarasov S.Yu. Controlling the porosity using exponential decay heat input regimes during electron beam wire-feed additive manufacturing of Al-Mg alloy. *International Journal of Advanced Manufacturing Technology*, 2020, vol. 108, pp. 2823–2838. DOI: 10.1007/s00170-020-05539-9.

19. Zhang X., Shi H., Wang X., Zhang S., Luan P., Hu X., Xu C. Processing, microstructure, and mechanical behavior of AZ31 magnesium alloy fabricated by electron beam additive manufacturing. *Journal of Alloys and Compounds*, 2023, vol. 938, p. 168567. DOI: 10.1016/j.jallcom.2022.168567.

20. Wolf T., Fu Z., Körner C. Selective electron beam melting of an aluminum bronze: microstructure and mechanical properties. *Materials Letters*, 2019, vol. 238, pp. 241–244. DOI: 10.1016/j.matlet.2018.12.015.

21. Zykova A.P., Panfilov A.O., Chumaevskii A.V., Vorontsov A.V., Nikonov S.Yu., Moskvichev E.N., Gurianov D.A., Savchenko N.L., Tarasov S.Yu., Kolubaev E.A. Formation of microstructure and mechanical characteristics in electron beam additive manufacturing of aluminum bronze with an in-situ adjustment of the heat input. *Russian Physics Journal*, 2022, vol. 65, iss. 5, pp. 811–817. DOI: 10.1007/s11182-022-02701-6.

22. Filippov A., Shamarin N., Moskvichev E., Savchenko N., Kolubaev E., Khoroshko E., Tarasov S. The effect of heat input, annealing, and deformation treatment on structure and mechanical properties of electron beam additive manufactured (EBAM) silicon bronze. *Materials*, 2022, vol. 15, p. 3209. DOI: 10.3390/ma15093209.

23. Khoroshko E.S., Filippov A.V., Shamarin N.N., Moskvichev E.N., Utyaganova V.R., Tarasov S.Yu., Savchenko N.L., Kolubaev E.A., Rubtsov V.E., Lychagin D.V. Structure and mechanical properties of Cu–Al–Si–Mn system-based copper alloy obtained by additive manufacturing. *Russian Physics Journal*, 2021, vol. 64, pp. 333–339. DOI: 10.1007/s11182-021-02333-2.

24. Casting of copper and copper alloys. *ASM Handbook*. Vol. 15. ASM International, 2008, pp. 1026–1048.

25. Sakai T., Belyakov A., Kaibyshev R., Miura H., Jonas J.J. Dynamic and post-dynamic recrystallization under hot, cold and severe plastic deformation conditions. *Progress in Materials Science*, 2014, vol. 60, pp. 130–207. DOI: 10.1016/j.pmatsci.2013.09.002.

26. Ponweiser N., Richter K.W. New investigation of phase equilibria in the system Al–Cu–Si. *Journal of Alloys and Compounds*, 2012, vol. 512, pp. 252–263. DOI: 10.1016/j.jallcom.2011.09.076.

27. Iqbal J., Ahmed F., Hasan F. Development of microstructure in silicon-aluminum-bronze. *Pakistan Journal of Engineering and Applied Sciences*, 2008, vol. 3, pp. 47–53.

28. Miettinen J. Thermodynamic description of the Cu–Al–Si system in the copper-rich corner. *Calphad*, 2007, vol. 31, pp. 449–456. DOI: 10.1016/j.calphad.2007.05.001.

29. Hisatsune C. Constitution diagram of the copper–silicon–aluminium system. *Memoirs of the College of Engineering, Kyoto Imperial University*, 1935, vol. 9, pp. 18–47.

30. Wilson F.H. The copper-rich corner of the copper-aluminum-silicon diagram. *Metals Technology*, 1948, vol. 15, pp. 1–12.

31. Hallstedt B., Gröbner J., Hampl M., Schmid-Fetzer R. Calorimetric measurements and assessment of the binary Cu–Si and ternary Al–Cu–Si phase diagrams. *Calphad*, 2016, vol. 53, pp. 25–38.

Conflicts of Interest

The authors declare no conflict of interest.